

Dynamic strain-field hysteresis model for ferromagnetic shape memory Ni-Mn-Ga

Neelesh N. Sarawate^a, Marcelo J. Dapino^a

^a Department of Mechanical Engineering,
The Ohio State University, Columbus, OH, USA, 43210

ABSTRACT

Due to magnetic field diffusion and structural dynamics, the relationship between magnetic field and strain in Ni-Mn-Ga changes significantly as the frequency of applied field is increased. In order to describe this behavior, which is critical for actuator applications, we present a strain model for Ni-Mn-Ga driven with dynamic magnetic fields. The magnitude and phase of the magnetic field inside the sample are modeled as a 1-D magnetic diffusion problem, from where an averaged or effective field is calculated. A continuum thermodynamics constitutive model is used to quantify the hysteretic response of the martensite volume fraction due to this effective magnetic field. The evolution of volume fractions with effective field is proposed to behave as a zero order system. To quantify the dynamic strain output, the actuator is represented as a lumped-parameter 1-DOF resonator with force input dictated by the twin-variant volume fraction. This results in a second order, linear ODE whose periodic force input is expressed as a summation of Fourier series terms. The total dynamic strain output is obtained by superposition of strain solutions due to each harmonic force input. The model accurately describes experimental measurements at frequencies of up to 250 Hz.

Keywords: Ferromagnetic shape memory alloys, Ni-Mn-Ga, dynamic actuation

1. INTRODUCTION

Ferromagnetic shape memory alloys in the Ni-Mn-Ga system produce 6% strain by magnetic field induced twin variant rearrangement. This strain is two orders of magnitude larger than the strain produced by magnetostrictive and piezoelectric materials. Due to the magnetic field activation, these materials exhibit faster response than thermally activated shape memory materials with comparable deformation response. The large strain and broad frequency bandwidth makes Ni-Mn-Ga an attractive material for dynamic actuator applications. Although considerable experimental and analytical work has been reported on the dependence of strain on static magnetic fields,^{1,2} work aimed at understanding the relationship between strain and dynamic magnetic fields has been scarce. This issue is created in part by the electromagnet device used to drive this material, which can in some cases suffer from limited frequency bandwidth due to high electrical inductance.

Henry³ presented measurements of magnetic field induced strains for drive frequencies of up to 250 Hz and a linear model to describe the phase lag between strain and field and system resonance frequencies. Petersen⁴ presented dynamic actuation measurements on piezoelectrically assisted twin boundary motion in Ni-Mn-Ga. The acoustic stress waves produced by a piezoelectric actuator complement the applied fields and allow for reduced field strengths. Scoby and Chen⁵ presented a preliminary magnetic diffusion model for cylindrical Ni-Mn-Ga material with the field applied along the long axis, but they did not quantify the dynamic strain response.

For modeling of dynamic piezoelectric or magnetostrictive transducers, the actuator dynamics must be coupled with the applied electric or magnetic fields through models for the strain generated by the active driver. This is often done by considering a spring-mass-damper resonator subjected to a forcing function which is proportional to the active strain. The active strain is related to the field by constitutive relations which can be linearized, without significant loss of accuracy, when a suitable bias field is present.⁶ However, the actuation response of

Further author information: (Send correspondence to M.J.D)

N.N.S.: E-mail: sarawate.1@osu.edu, Telephone: 1-614-247-7480

M.J.D.: E-mail: dapino.1@osu.edu, Telephone: 1-614-688-3689

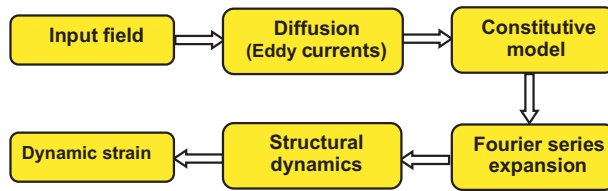


Figure 1. Flow chart for modeling of dynamic Ni-Mn-Ga actuators.

Ni-Mn-Ga is dictated by the rearrangement of martensite twin variants, which are either field-preferred or stress-preferred depending on whether the magnetically easy crystal axis is aligned with field or stress. The evolution of twin variants with a.c. magnetic fields always exhibit large hysteresis, hence the constitutive strain-field relation of Ni-Mn-Ga cannot be accurately quantified by linearized models.

This paper quantifies the hysteretic relationship between magnetic fields and strains in dynamic actuators consisting of a Ni-Mn-Ga element, return spring, and external mechanical load. The key contribution of this paper is the modeling of coupled structural and magnetic dynamics in Ni-Mn-Ga actuators by means of a simple (yet accurate) framework. The framework constitutes a useful tool for the design of actuators with straightforward geometries and provides a set of core equations for finite element solvers applicable to more complex geometries. Further, it offers the possibility of obtaining input field profiles that produce a prescribed strain profile, which can be a useful tool in actuator control.

The model is focused on describing properties of measured Ni-Mn-Ga data³ observed as the frequency of the applied magnetic field is increased, as follows: (1) For a given a.c. voltage magnitude, the maximum current and associated maximum applied field decrease due to an increase in the impedance of the coils; (2) The field at zero strain (i.e., field required to change the sign of the deformation rate) increases over a defined frequency range, indicating an increasing phase lag of the strain relative to the applied field; and (3) For a given applied field magnitude, the maximum strain magnitude decreases and the shape of the hysteresis loop changes significantly. We posit that overdamped second-order structural dynamics and magnetic field diffusion due to eddy currents are the primary causes for the observed behaviors. The two effects are coupled: eddy currents reduce the magnitude and delays the phase of the magnetic field towards the center of the material, which in turn affects the corresponding strain response through the structural dynamics (Figure 1). Magnetization dynamics and twin boundary motion response times are considered relatively insignificant.

The model is constructed as illustrated in Figure 1. First, the magnitude and phase of the magnetic field inside a prismatic Ni-Mn-Ga sample are modeled as a 1-D magnetic diffusion problem with applied a.c. fields known on the surface of the sample. To calculate the bulk magnetic field-induced deformation, an effective or average magnetic field acting on the material is calculated. With this effective field, a previous continuum thermodynamics constitutive model^{7,8} is used to quantify the hysteretic response of the martensite volume fraction. The evolution of the volume fraction defines an equivalent forcing function dependent on the elastic modulus of the Ni-Mn-Ga sample, its cross-sectional area, and the maximum reorientation strain. Assuming steady-state excitation, this forcing function is periodic and can be expressed as a Fourier series. This Fourier series provides the force excitation to a lumped-parameter 1-DOF resonator representing the Ni-Mn-Ga actuator. The dynamic strain response is obtained by superposition of the strain response to forces of different frequencies.

For model validation, dynamic measurements presented by Henry³ are utilized. A 10 mm × 10 mm × 20 mm single crystal Ni-Mn-Ga sample was placed between the poles of an E-shaped electromagnet with the 10 mm × 20 mm sides facing the magnet poles. The magnetic field was applied perpendicular to the longitudinal axis of the material, which tends to elongate the sample. A spring of stiffness 36 kN/m provided a compressive bias stress of 1.7 MPa along the longitudinal axis of the sample to achieve reversible field-induced actuation in response to cyclic fields. Figure 2 shows dynamic actuation measurements. The strain response of Ni-Mn-Ga depends on the magnitude of the applied field but not on its direction, thus giving two strain cycles per field cycle. The frequencies shown in Figure 2 are the inverse of the time period of one strain cycle. Thus, the

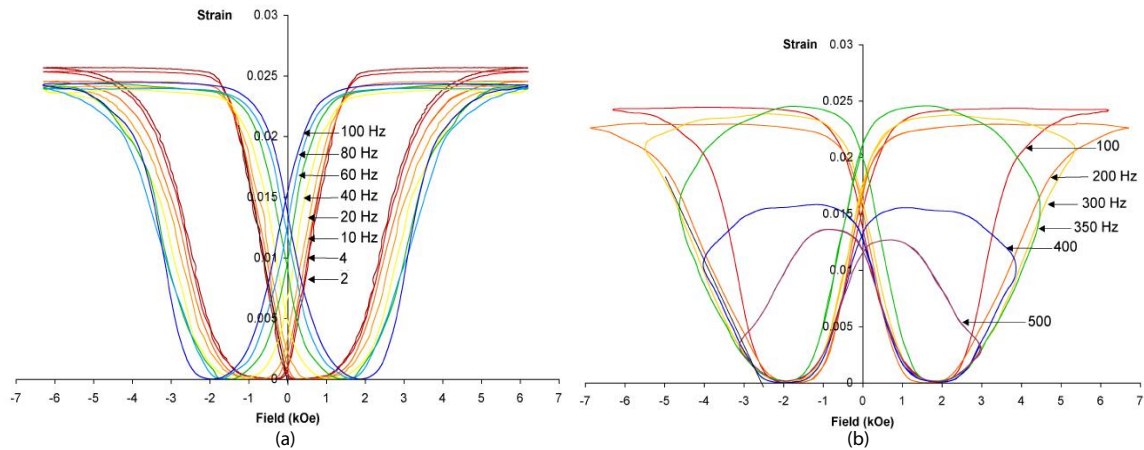


Figure 2. Dynamic actuation data by Henry³ for 2 – 100 Hz ($f_a = 1 - 50$ Hz) and 100 – 500 Hz ($f_a = 50 - 250$ Hz).

frequency of applied field ranges from 1-250 Hz. It is also noted that the applied field amplitude decays with increasing frequency, likely due to a combination of high electromagnet inductance and the measurements having been conducted at constant voltage rather than at constant current.

Since the experimental magnetic field waveform is not described in Henry's thesis,³ sinusoidal and triangular waveforms are studied. It is proposed that the experimental field waveform deviates from an exact waveform (sinusoidal or triangular) as the applied field frequency increases. Nonetheless, study of these two ideal waveforms provides insight on the physical experiments.

2. MAGNETIC FIELD DIFFUSION

The application of an alternating magnetic field to a conducting material results in the generation of eddy currents and an internal magnetic field which partially offsets the applied field. The relationship between the eddy currents and applied fields is described by Maxwell's electromagnetic equations. Assuming that the magnetization is uniform and does not saturate, the diffusion equation describing the magnetic field inside a one-dimensional conducting medium has the form⁹

$$\nabla^2 H - \mu \bar{\sigma} \frac{\partial H}{\partial t} = 0, \quad (1)$$

where $\bar{\sigma}$ is the conductivity, μ is the magnetic permeability, and $\bar{\epsilon}$ is the dielectric constant. The assumption of uniform magnetization is not necessarily met experimentally due to nonuniform twin boundary motion¹⁰ and saturation effects. However, comparison of model results and measurements (Section IV) suggests that the simplified diffusion model is able to describe the problem qualitatively. This is attributed to the susceptibilities of field-preferred and stress-preferred variants being relatively close (4.7 and 1.1, respectively⁷) and not differing too much from zero as twin boundary motion and magnetization rotation processes take place. It is also speculated that the variants are sufficiently fine in the tested material.

The solution to (1) gives the magnetic field values $H(\bar{x}, t)$ at position \bar{x} (inside a material of thickness $2d$) and time t . The boundary condition at the two ends is the externally applied magnetic field. In the case of harmonic fields, the boundary condition is given by

$$H(\pm d, t) = H_0 e^{i\omega t} \quad (2)$$

where H_0 is the amplitude and $\omega = 2\pi f_a$ is the circular frequency (rad/s) of the magnetic field on the surface of the Ni-Mn-Ga sample. Assuming no leakage flux in the gap between the electromagnet and sample, this field is the same as the applied field. The solution for magnetic fields inside the material has the form⁹

$$H(\bar{x}, t) = H_0 h(\bar{X}) e^{i\omega t}. \quad (3)$$

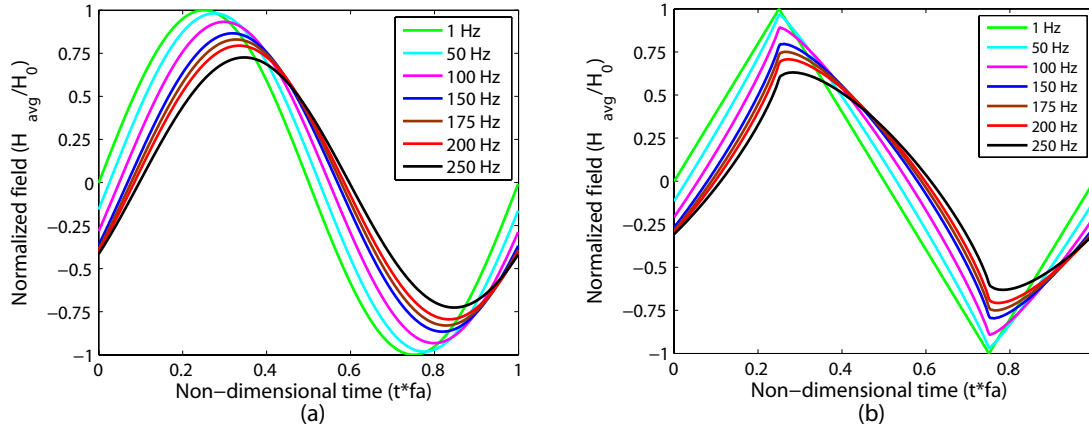


Figure 3. Average field waveforms with increasing actuation frequency for (a) sinusoidal input and (b) triangular input.

In this expression, the complex magnitude scale factor is

$$\begin{aligned}
 h(\bar{X}) &= A(B + iC), \\
 A &= \frac{1}{\cosh^2 \bar{X}_d \cos^2 \bar{X}_d + \sinh^2 \bar{X}_d \sin^2 \bar{X}_d}, \\
 B &= \cosh \bar{X} \cos \bar{X} \cosh \bar{X}_d \cos \bar{X}_d + \sinh \bar{X} \sin \bar{X} \sinh \bar{X}_d \sin \bar{X}_d, \\
 C &= \sinh \bar{X} \sin \bar{X} \cosh \bar{X}_d \cos \bar{X}_d - \cosh \bar{X} \cos \bar{X} \sinh \bar{X}_d \sin \bar{X}_d,
 \end{aligned} \tag{4}$$

with

$$\bar{X} = \bar{x}/\delta, \bar{X}_d = d/\delta, \delta = \sqrt{\frac{2}{\omega \mu \sigma}}, \tag{5}$$

where δ is the skin depth, or the distance inside material at which the diffused field is $1/e$ times the external field. To estimate the effective magnetic field, an average of the field waveforms at various positions is calculated,

$$H_{\text{avg}}(t) = \frac{1}{N_x} \sum_{\bar{X}=-\bar{X}_d}^{\bar{X}_d} H_0 h(\bar{X}) e^{i\omega t}. \tag{6}$$

Here, N_x represents the number of uniformly spaced points inside the material where the field waveforms are calculated.

If the external field is an arbitrary periodic function, the corresponding boundary condition is represented as a Fourier series expansion. The diffused internal field is then obtained by superposition of individual solutions (3) to each harmonic component of the applied field.

Figure 3 shows averaged field waveforms at several applied field frequencies for sinusoidal and triangular inputs. In these simulations the resistivity has a value of $\bar{\rho} = 1/\bar{\sigma} = 6\text{e-}8$ Ohm-m and the relative permeability is $\mu_r = 3$. At 1 Hz, the magnetic field intensity is uniform throughout the material and equal to the applied field H_0 , and there is no phase lag. With increasing actuation frequency, the magnetic field diffusion results in a decrease in the amplitude and an increase in the phase lag of the averaged field relative to the field on the surface of the material. Figure 4 shows the decay of the magnetic field amplitude with position inside the material at several applied field frequencies.

When the applied field is sinusoidal, the diffused average field is also sinusoidal regardless of frequency (Figure 3a). When the applied field is triangular, the shape of the diffused average field increasingly differs from the input field as the frequency is increased (Figure 3b). The corresponding strain waveforms are modified accordingly as they are dictated by the material response to the effective averaged field. Thus, the shape of the input field waveform can alter the final strain profile. This is discussed in section 4.

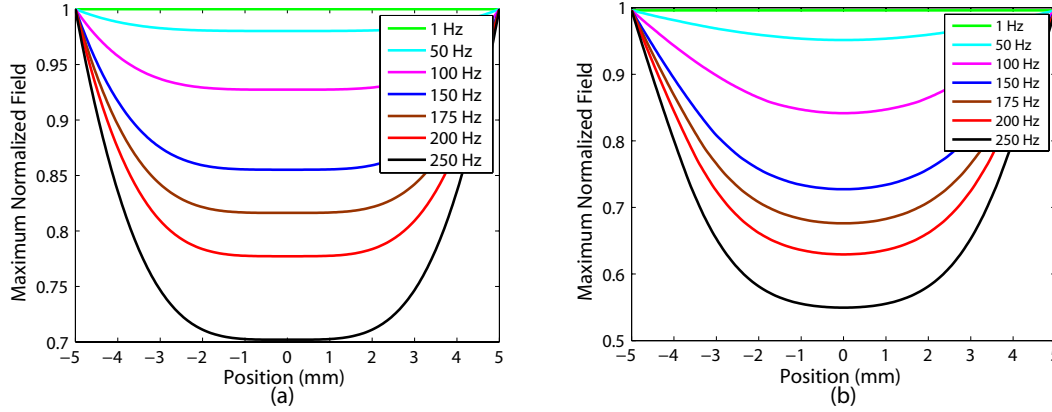


Figure 4. Dependence of normalized field amplitude on position with increasing actuation frequency for (a) sinusoidal input and (b) triangular input.

3. QUASISTATIC STRAIN-FIELD HYSTERESIS MODEL

Our previous magnetomechanical model^{7,8} is used to obtain constitutive material response. The model incorporates thermodynamic potentials to define reversible processes in combination with evolution equations for internal state variables associated with dissipative effects. The model naturally quantifies the actuation or sensing effects depending on which variable pairs among stress, strain, magnetic field, and magnetization, are selected as independent and dependent variables. In this section we focus on the essential components of the model, while further details on its development can be found in.^{7,8} For the actuation problem under consideration, the average or effective field H_{avg} (for simplicity denoted H from now on) and bias compressive stress σ_b are the independent variables, and the strain ε and magnetization M are the dependent variables.

The simplified twin variant microstructure for single crystal Ni-Mn-Ga is shown in Figure 5. The magnetic field and the applied stress (or strain) are oriented in x and y direction respectively. A field-preferred variant, with volume fraction ξ , is one in which the magnetically easy c -axis is aligned with the x direction. A stress-preferred variant, with volume fraction $1 - \xi$, is one in which the c -axis is aligned in the y direction. It is assumed that the variant volume fractions are sufficiently large to be subdivided into 180-degree magnetic domains with volume fractions α and $1 - \alpha$. This domain structure minimizes the net magnetostatic energy. The high magnetocrystalline energy of Ni-Mn-Ga dictates that the magnetization vectors in the field-preferred variant are attached to the crystallographic c -axis, whereas the magnetization vectors in the stress-preferred variant are rotated an angle θ relative to the c -axis. Energy minimization dictates that this angle is equal and opposite in the two magnetic domains within a stress-preferred variant. The magnetization component in the x direction is found by inspection to be

$$M(\xi, \alpha, \theta) = M_s[2\xi\alpha - \xi + \sin\theta - \xi\sin\theta], \quad (7)$$

where M_s is the saturation magnetization. The modified Clausius-Duhem inequality for the actuation problem is written as

$$-\rho\dot{\phi} - \dot{\sigma}_b\varepsilon_e - \mu_0\dot{H}M + \sigma_b\varepsilon_{tw} \geq 0. \quad (8)$$

Here, ρ is density, ϕ is specific Gibbs energy, ε_e is elastic strain component, ε_{tw} is twinning strain component, and μ_0 is permeability of free space. The elastic and twinning strain are the two components of the total strain exhibited by the material, with the twinning strain being proportional to the field-preferred volume fraction,

$$\varepsilon = \varepsilon_e + \varepsilon_{tw} = \varepsilon_e + \varepsilon_0\xi, \quad (9)$$

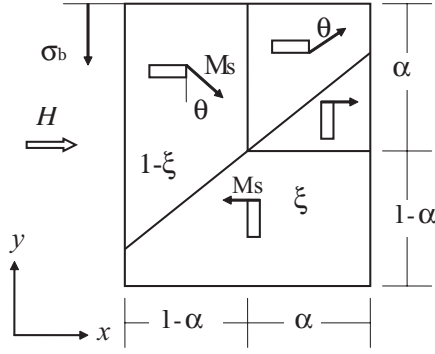


Figure 5. Simplified twin variant microstructure in Ni-Mn-Ga.

where ε_0 is the maximum reorientation strain. The constitutive equations for the elastic strain component and magnetization are given as,

$$\varepsilon_e = \frac{\partial(\rho\phi)}{\partial\sigma_b}, \quad M = -\frac{1}{\mu_0} \frac{\partial(\rho\phi)}{\partial H}. \quad (10)$$

The total Gibbs energy is expressed as a summation of magnetic and mechanical energies. The magnetic Gibbs energy consists of Zeeman, magnetostatic, and anisotropy energy contributions. The Zeeman energy represents the work done by external magnetic fields on the material, or the energy available to drive the twin boundary motion with magnetic fields. The magnetostatic energy is associated with the demagnetization field created inside the material due to finite dimensions of the sample. The demagnetization field tends to oppose the applied field, and the magnetostatic energy tends to reduce the net magnetization inside the material to zero. The anisotropy energy represents the energy associated with pure rotation of the magnetization vectors (hard axis) compared to the magnetization due to zero rotation of vectors (easy axis). The total magnetic energy is expressed as the weighted sum of the energies of the two variants represented in Figure 5,

$$\begin{aligned} \rho\phi_{mag} = & \xi[-\mu_0 H M_s \alpha + \mu_0 H M_s (1-\alpha) + \frac{1}{2} \mu_0 N (M_s \alpha - M_s (1-\alpha))^2] \\ & + (1-\xi)[- \mu_0 H M_s \alpha \sin \theta + \frac{1}{2} \mu_0 N M_s^2 \sin^2 \theta + K_u \sin^2 \theta], \end{aligned} \quad (11)$$

in which N is the demagnetization factor and K_u is the magnetocrystalline anisotropy constant.

The mechanical Gibbs energy includes elastic and twinning contributions. The mechanical energy varies depending on whether the field is increasing or decreasing,

$$\begin{aligned} \rho\phi_{mech} = & -\frac{1}{2E} \sigma_b^2 + \frac{1}{2} a \varepsilon_0^2 (\xi - \xi_s) \quad (\dot{H} > 0), \\ \rho\phi_{mech} = & -\frac{1}{2E} \sigma_b^2 + \frac{1}{2} a \varepsilon_0^2 (\xi - \xi_f + \xi_s) \quad (\dot{H} < 0), \end{aligned} \quad (12)$$

with E the elastic modulus, a the modulus associated with the twinning strain,⁷ ξ_s the volume fraction at the start of the actuation process, and ξ_f the volume fraction at the end of actuation. The magnetization process in single crystal Ni-Mn-Ga is assumed to be reversible, hence the thermodynamic driving forces associated with the domain fraction (π^α) and magnetization rotation angle (π^θ) are zero,

$$\pi^\alpha = -\frac{\partial(\rho\phi)}{\partial\alpha} = 0, \quad \pi^\theta = -\frac{\partial(\rho\phi)}{\partial\theta} = 0. \quad (13)$$

This yields closed form solutions for the domain fraction and rotation angle which have the form

$$\alpha = \frac{H}{2NM_s} + \frac{1}{2}, \quad \theta = \sin^{-1} \left(\frac{\mu_0 H M_s}{\mu_0 N M_s^2 + 2K_u} \right), \quad (14)$$

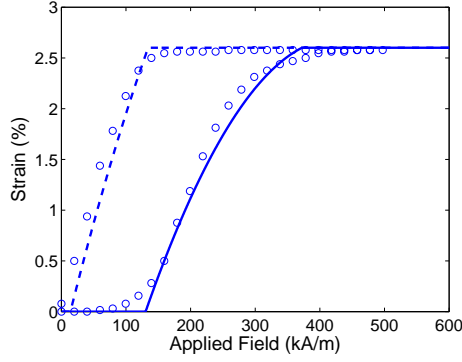


Figure 6. Model result for quasistatic strain vs. magnetic field. The circles denote experimental data points (1 Hz line in Figure 2) while the solid and dashed lines denote model simulations for $\dot{H} > 0$ and $\dot{H} < 0$, respectively.

subject to the constraints $0 \leq \alpha \leq 1$ and $-\pi/2 \leq \theta \leq \pi/2$. The Clausius-Duhem inequality (8) is reduced to

$$\left(-\frac{\partial(\rho\phi)}{\partial\xi} + \sigma_b\varepsilon_0\right)\dot{\xi} \geq 0, \quad (15)$$

and the net thermodynamic driving force ($\pi^{\xi*}$) is thus given by

$$\pi^{\xi*} = -\frac{\partial(\rho\phi)}{\partial\xi} + \sigma_b\varepsilon_0 = \pi^\xi + \sigma_b\varepsilon_0. \quad (16)$$

When a magnetic field is applied, twin boundary motion starts when the net thermodynamic driving force exceeds a critical value $\pi^{cr} = \sigma_{tw0}\varepsilon_0$, where σ_{tw0} is the twinning stress required to initiate twin boundary motion when the material is compressed from its maximum length ($\xi = 1$). For decreasing field, the critical force to be overcome is π^{-cr} . The volume fraction is obtained by numerically solving the piecewise continuous equations,

$$\begin{aligned} \pi^{\xi*} &= \pi^{cr} & (\dot{H} \geq 0), \\ \pi^{\xi*} &= -\pi^{cr} & (\dot{H} \leq 0). \end{aligned} \quad (17)$$

The volume fraction is thus given by

$$\begin{aligned} \xi &= \frac{\pi_{mag}^\xi + \sigma_b\varepsilon_0 + a\varepsilon_0^2\xi_s - \pi^{cr}}{a\varepsilon_0^2} & (\dot{H} \geq 0), \\ \xi &= \frac{\pi_{mag}^\xi + \sigma_b\varepsilon_0 + a\varepsilon_0^2\xi_f - a\varepsilon_0^2\xi_s + \pi^{cr}}{a\varepsilon_0^2} & (\dot{H} \leq 0), \end{aligned} \quad (18)$$

where $\pi_{mag} = -\partial(\rho\phi_{mag})/\partial\xi$ is the thermodynamic driving force associated with the applied magnetic field. Thus, inequality (15) is satisfied during the entire process.

Figure 6 shows a comparison of model results with actuation data for a 1 Hz applied field. The model parameters used are: $\varepsilon_0 = 0.04$, $k = 70$ MPa, $M_s = 0.8$ T, $K_u = 1.7$ J/m³, and $\sigma_{tw0} = 0.5$ MPa. The hysteresis loop in Figure 6 is dominated by the twinning strain $\varepsilon_0\xi$ (proportional to volume fraction), which represents around 99% of the total strain. The variation of volume fraction with effective field is proposed to behave as a zero order system, without any dynamics of its own, and thus independent of the frequency of actuation. The second order structural dynamics associated with the transducer vibrations modify the constitutive behavior shown in Figure 6 in the manner detailed in section 4.

4. DYNAMIC ACTUATOR MODEL

The average field H_{avg} (denoted H for simplicity) acting on the Ni-Mn-Ga sample is calculated by applying expression (6) to a given input field waveform. Using this effective field, the actuator model described in section 3 is used to calculate the field-preferred martensite volume fraction ξ . By ignoring the dynamics of twin boundary motion, the dependence of volume fraction on applied field given by relations (18) is that of a zero-order system ($\xi = f[H(t)]$). Marioni et. al.¹¹ studied the actuation of Ni-Mn-Ga single crystal using magnetic field pulses lasting 620 μs . It was observed that the full 6% magnetic field induced strain was obtained in less than 250 μs implying that the bandwidth of the Ni-Mn-Ga element was around 2000 Hz. As the frequencies in the present work are below 250 Hz, one can accurately assume that twin boundary motion, and hence the evolution of volume fractions, occurs in concert with the applied field according to the dynamics of a zero-order system.

The mechanical properties of a dynamic Ni-Mn-Ga actuator are illustrated in Figure 7. Although the position of twin boundaries in the crystal affects the inertial response of the material,¹¹ this effect is ignored with the assumption of a lumped mass system. The actuator is modeled as a 1-DOF, lumped-parameter resonator in which the Ni-Mn-Ga rod acts as an equivalent spring of stiffness EA/L , with E the modulus, A the area, and L the length of the Ni-Mn-Ga sample. This equivalent spring is in parallel with the load spring of stiffness k , which is also used to pre-compress the sample. The overall system damping is represented by c and the combined mass of the Ni-Mn-Ga sample and output pushrod are modeled as a lumped mass m . When an external field $H_a(t)$ is applied to the Ni-Mn-Ga sample, an equivalent force $F(t)$ is generated which drives the motion of mass m .

We employ an approach similar to that used for the modeling of dynamic magnetostrictive actuators. The motion of mass m is represented by a second order differential equation,

$$m\ddot{x} + c\dot{x} + kx = F(t) = -\sigma(t)A, \quad (19)$$

with x the displacement of mass m . An expression for the normal stress is obtained from (9) and (10) as

$$\sigma = E(\varepsilon - \varepsilon_0\xi) = E\left(\frac{x}{L} - \varepsilon_0\xi\right). \quad (20)$$

The bias strain resulting from initial and final volume fractions (ξ_s, ξ_f) is compensated for when plotting the total strain. Substitution of (20) into (19) gives

$$m\ddot{x} + c\dot{x} + \left(k + \frac{AE}{L}\right)x = AE\varepsilon_0\xi. \quad (21)$$

Equation (21) represents a second-order dynamic system driven by the volume fraction. The dependence of volume fraction on applied field given by relations (18) is nonlinear and hysteretic, and follows the dynamics of a zero-order system, i.e., the volume fraction does not depend on the frequency of the applied magnetic field. This is in contrast to biased magnetostrictive actuators, in which the drive force can be approximated by a linear function of the magnetic field since the amount of hysteresis in minor magnetostriction loops often is significantly less than in Ni-Mn-Ga.

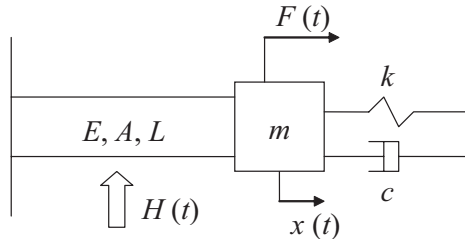


Figure 7. Dynamic Ni-Mn-Ga actuator consisting of an active sample (spring) connected in mechanical parallel with an external spring and damper. The mass includes the dynamic mass of the sample and the actuator's output pushrod.

For periodic applied fields, the volume fraction also follows a periodic waveform and hence the properties of Fourier series are utilized to calculate model solutions. Figure 8 shows the calculated variation of volume fraction with time for the cases of sinusoidal and triangular external fields. The reconstructed waveforms shown in the figure are discussed later.

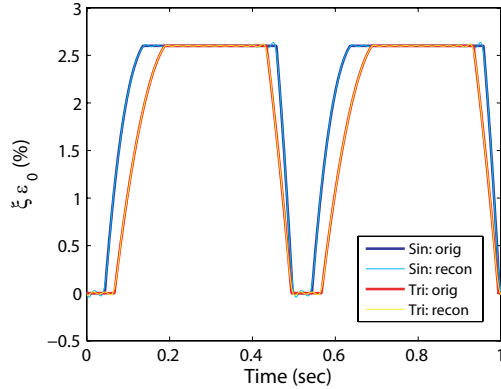


Figure 8. Volume fraction profile vs. time ($f_a = 1$ Hz).

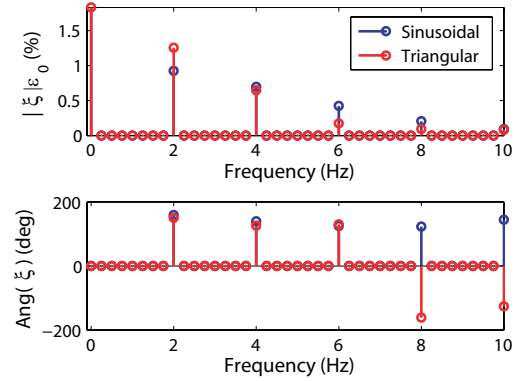


Figure 9. Single sided frequency spectrum of volume fraction ($f_a = 1$ Hz).

Using a Fourier series expansion, the periodic volume fraction is represented as a sum of sinusoidal functions. The Fourier coefficients are

$$\bar{Z}_k = \frac{1}{T_a} \int_0^{T_a} \xi(t) e^{-i\omega_k t} dt, \quad k = 0, \pm 1, \pm 2, \dots \quad (22)$$

where $T_a = 1/f_a$, with f_a the fundamental frequency. The frequency spectrum of the volume fraction thus consists of discrete components at the frequencies $\pm\omega_k, k = 0, 1, 2, \dots$; \bar{Z}_k is the complex Fourier coefficient corresponding to the k^{th} harmonic. Equation (22) yields a double sided discrete frequency spectrum consisting of frequencies $-f_s/2 \dots f_s/2$, where $f_s = 1/dt$ represents the sampling frequency which depends on the time domain resolution dt of the signal. The double sided frequency spectrum is converted to a single sided spectrum through the relations

$$\begin{aligned} |Z_0| &= |\bar{Z}_0| & k &= 0, \\ |Z_k| &= |\bar{Z}_k| + |\bar{Z}_{-k}| = 2|\bar{Z}_k| & k &> 0. \end{aligned} \quad (23)$$

The phase angles remain unchanged,

$$\angle Z_k = \angle \bar{Z}_k \quad k \geq 0. \quad (24)$$

The reconstructed volume fraction $\bar{\xi}_r(t)$ is

$$\bar{\xi}_r(t) = \bar{\xi}_r(t \pm T_a) = \sum_{k=-K}^K \bar{Z}_k e^{i\omega_k t}, \quad (25)$$

in which K represents the number of terms in the series. The single sided frequency spectrum of the volume fraction is shown in Figure 9 for sinusoidal and triangular applied field waveforms. This spectrum consists of frequencies $0 \dots f_s/2$. It is noted that the plotted spectrum has a resolution of $df = f_a/4$, as four cycles of the applied field are included. The actuation frequency in the presented case is $f_a = 1$ Hz. For an input field frequency of f_a Hz, the volume fraction spectrum consists of non-zero components at frequencies $2f_a, 4f_a, 6f_a, \dots$ Hz. Mathematically, the phase angles appear to be leading; the physically correct phase angle values are obtained by subtracting π from the mathematical values.

Finally, if the applied field has the form

$$H_a(t) = H_0 \sin(2\pi f_a t), \quad (26)$$

with H_0 constant, then the reconstructed volume fraction $\xi_r(t)$ is represented in terms of the single sided Fourier coefficients by

$$\xi_r(t) = \xi_r(t \pm T_a) \sum_{k=0}^K |Z_k| \cos(2\pi k f_a t + \angle Z_k). \quad (27)$$

The reconstructed volume fraction signal overlapped over the original is shown in Figure 8, for both the sinusoidal and triangular input fields. The number of terms used is $K = 20$. Substitution of (27) into (21) gives

$$m\ddot{x} + c\dot{x} + (k + \frac{AE}{L})x = AE\varepsilon_0 \sum_{k=0}^K |Z_k| \cos(2\pi k f_a t + \angle Z_k), \quad (28)$$

which represents a second-order dynamic system subjected to simultaneous harmonic forces at the frequencies $k f_a$, $k = 0, \dots, K$. The steady state solution for the net displacement $x(t)$ is given by the superposition of steady state solutions to each forcing function. Thus, the steady state solution for the dynamic strain ε_d has the form

$$\varepsilon_d(t) = \frac{x(t)}{L} = \frac{EA\varepsilon_0}{EA + kL} \sum_{k=0}^K |Z_k| |X_k| \cos(2\pi k f_a t + \angle Z_k - \angle X_k). \quad (29)$$

In (29), X_k represents the non-dimensional transfer function relating the force at the k^{th} harmonic and the corresponding displacement,

$$X_k = \frac{1}{[1 - (k f_a / f_n)^2] + j(2\zeta k f_a / f_n)} = |X_k| e^{-i\angle X_k} \quad (30)$$

where

$$|X_k| = \frac{1}{\sqrt{[1 - (k f_a / f_n)^2]^2 + (2\zeta k f_a / f_n)^2}}, \quad \angle X_k = \tan^{-1}\left(\frac{2\zeta k f_a / f_n}{1 - (k f_a / f_n)^2}\right). \quad (31)$$

The natural frequency and damping ratio in these expressions have the form

$$f_n = \frac{1}{2\pi} \sqrt{\frac{k + AE/L}{m}}, \quad \zeta = \frac{c}{2\sqrt{(k + AE/L)m}}. \quad (32)$$

Figure 10 shows experimental and modeled strain versus field curves for sinusoidal and triangular waveforms at varied frequencies. The model parameters used are $f_n = 700$ Hz, $\zeta = 0.95$, $\rho = 62 \times 10^{-8}$ Ohm-m, and $\mu_r = 3$. The natural frequency is obtained by using a modulus of $E=166$ MPa, which is estimated from the stress-strain plots in.³ The dynamic mass of the Ni-Mn-Ga sample and pushrods is $m=0.027$ kg. It is seen that the assumption of triangular input field waveform tends to model the higher frequency data well. This implies that the shape of the applied field waveform may not remain exactly sinusoidal at higher frequencies. For example, the experimental data at 250 Hz shows a slight discontinuity when the applied field changes direction, thus verifying the proposed claim of triangular shape.

The model results match the experimental data well with the assumption of triangular input field waveform, except for the case of 200 Hz. This may be due to the influence of model parameters in that particular case. Otherwise, the model accurately predicts the increase of coercive field, the magnitude of maximum strain, and the overall shape change of the hysteresis loop with increasing actuation frequency. The lack of overshoot in the experimental data for any of the frequencies justifies the assumption of overdamped system. The average error between the experimental data and the model results is 2.37%, which increases to 4.24% in the case of $f_a = 200$ Hz. The relationship between strain and field is strongly nonlinear and hysteretic due to factors such as magnetic field diffusion, constitutive coupling, and structural dynamics.

Figure 11 shows a comparison of model results and experimental data in the frequency domain. Only the results for triangular input field waveform are shown, as the actual input field is proposed to be close to the triangular function from the simulations. The frequency spectrum of the experimental strain data shows a monotonous decay of strain magnitudes with increasing even harmonics up to an actuation frequency of 100

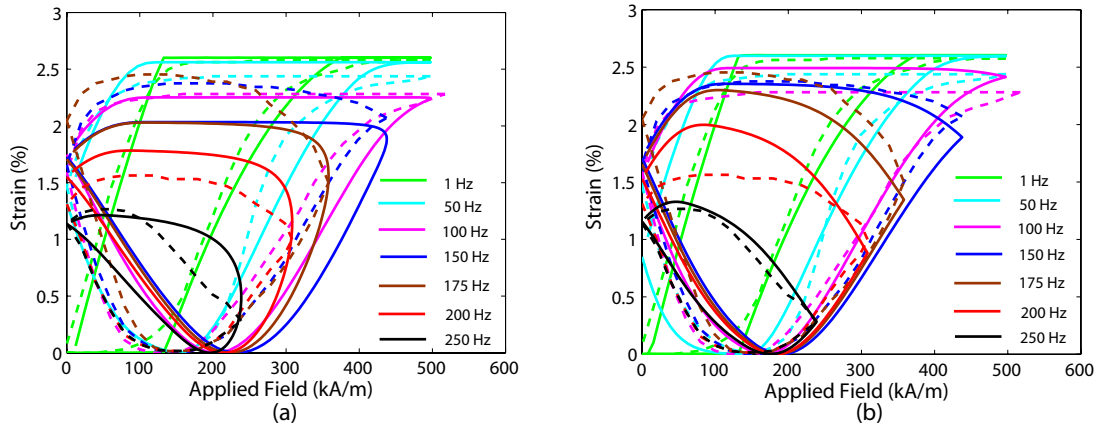


Figure 10. Model results for strain vs. applied field at different frequencies for (a) sinusoidal, (b) triangular input waveforms. Dotted line: experimental, solid line: model.

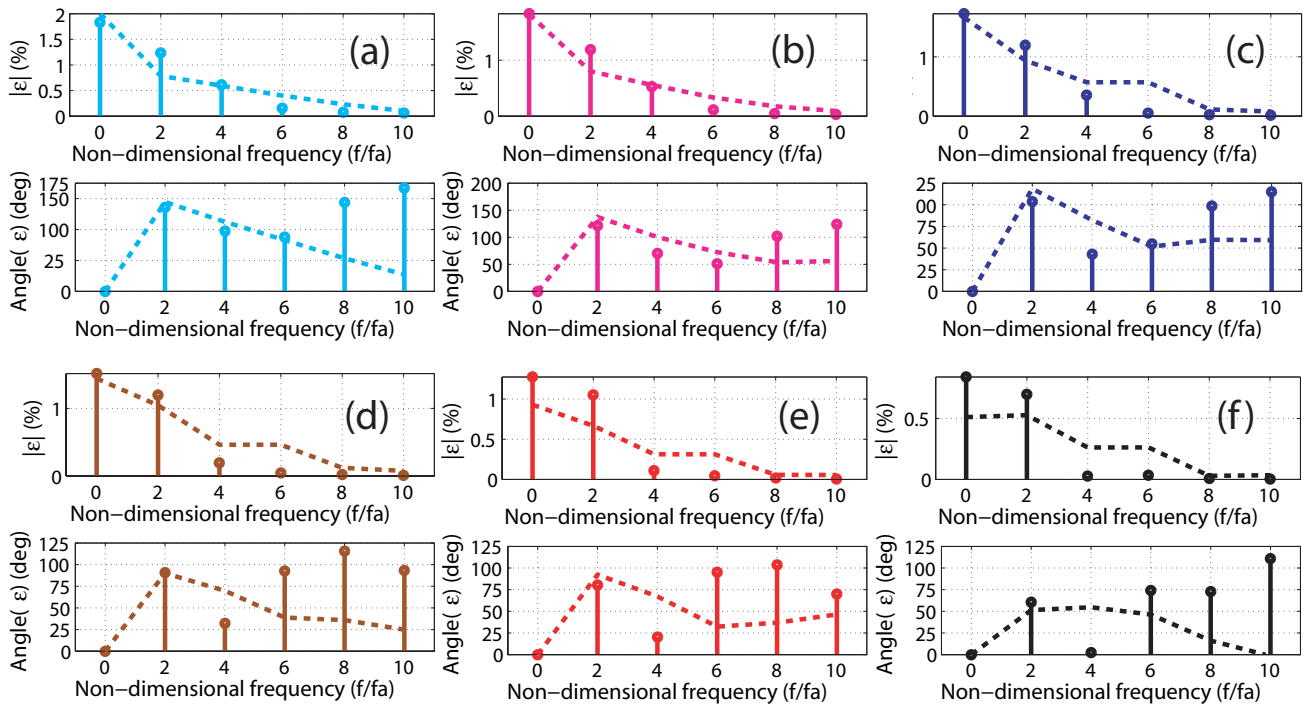


Figure 11. Model results for strain vs. applied field in frequency domain for triangular input waveform for (a) $f_a = 50$ Hz, (b) $f_a = 100$ Hz, (c) $f_a = 150$ Hz, (d) $f_a = 175$ Hz, (e) $f_a = 200$ Hz, (e) $f_a = 250$ Hz. Dotted line: experimental, solid line: model.

Hz. For actuation frequencies from 150 Hz onwards, the decay is not monotonous, for example, the strain magnitudes corresponding to the 4th and 6th harmonic are almost equal, with the magnitude corresponding to the 2nd harmonic being comparatively high. This behavior is reflected in the strain-field plots as the hysteresis loop shows increasing rounding-off for frequencies higher than 150 Hz. The model accurately describes these responses as the magnitudes match the experimental values well for most cases. The phase angles for the experimental and model spectra also show a good match. In some cases, the angles show a discrepancy of about 180 deg, though they are physically equivalent.

5. CONCLUSION

A model is presented to describe the dependence of strain on applied field at varied frequencies in ferromagnetic shape memory Ni-Mn-Ga. The essential components of the model include magnetomechanical constitutive responses, magnetic field diffusion, and structural dynamics. The presented method can be extended to arrive at the input field profiles which will result in the desired strain profile at a given frequency. If the direction of flow in Figure 1 is reversed, the input field profile can be designed from a desired strain profile. It is comparatively easy to obtain the inverse Fourier transform, whereas calculation of the average field from a desired strain profile through the constitutive model, and estimation of the external field from the averaged diffused field inside the sample can be complex.

The frequency spectra of the field preferred volume fraction and the resulting dynamic strain include even harmonics. The corresponding magnitudes at the 2nd harmonic are comparatively high indicating frequency doubling similar to that associated with magnetostrictive actuators. However, additional components at higher harmonics are present due to the large hysteresis in ferromagnetic shape memory alloys compared to biased magnetostrictive materials. If the overall system including the active material is underdamped, then it is possible to achieve system resonance at a frequency which is 1/4th or 1/6th of the system natural frequency. In magnetically-active material actuators, the application of magnetic fields at high frequencies becomes increasingly difficult as the coil inductances tend to increase rapidly. If the actuator can be made to resonate at a fraction of the system natural frequency, then this problem can be simplified. However, the strain magnitudes corresponding to the higher harmonics tend to diminish rapidly as well, which creates a compensating effect. Further, in some cases the natural frequency and damping of the system may be beyond the control of the designer. Nevertheless, our approach suggests a way to drive a magnetic actuator at a fraction of the natural frequency to achieve resonance.

Acknowledgement

Funding for N.N.S. comes from National Science Foundation through grant CMS-0409512, Dr. Shih-Chi Liu program director, and the Ohio State University through an NSF I/UCRC on Smart Vehicle Concepts graduate fellowship.

REFERENCES

1. O. Soderberg, Y. Ge, A. Sozinov, S. Hannula, and V. K. Lindroos, "Recent breakthrough development of the magnetic shape memory effect in NiMnGa alloys," *Smart Mater. Struct.* **14**, p. S223, 2005.
2. J. Kiang and L. Tong, "Modelling of magneto-mechanical behavior of NiMnGa single crystals," *J. Magn. Magn. Mater.* **292**, p. 394, 2005.
3. C. Henry, "Dynamic actuation properties of NiMnGa ferromagnetic shape memory alloys," *PhD Thesis, MIT*, 2002.
4. B. Petersen, "Acoustic assisted actuation of NiMnGa ferromagnetic shape memory alloys," *PhD Thesis, MIT*, 2006.
5. S. Scoby and Y. Chen, "Dynamic behavior of ferromagnetic shape memory alloys," *AIAA Struct. Dyn. Conf.* **1630**, p. 1768, 2006.
6. P. Downey and M. Dapino, "Extended frequency bandwidth and electrical resonance tuning in hybrid terfenol-D/PMN-PT transducers in mechanical series configuration," *J. Intel. Mater. Sys. Struct.* **16**, p. 757, 2005.
7. N. Sarawate and M. Dapino, "A continuum thermodynamics model for the sensing effect in ferromagnetic shape memory NiMnGa," *J. Appl. Phys.* **101**, p. 123522, 2007.
8. N. Sarawate and M. Dapino, "Magnetomechanical characterization and unified actuator/sensor modeling of ferromagnetic shape memory alloy NiMnGa," *Proc. SPIE* **6526**, p. 652629, 2007.
9. H. Knoopfel, *Magnetic Fields: A Comprehensive Theoretical Treatise*, John Wiley and Sons, 2000.
10. S. Murray, M. Marioni, A. Kukla, J. Robinson, R. O'Handley, and S. Allen, "Large field induced strain in single crystalline NiMnGa ferromagnetic shape memory alloy," *J. Appl. Phys.* **87**, p. 5774, 2000.
11. M. A. Marioni, R. C. O'Handley, and S. M. Allen, "Pulsed magnetic field-induced actuation of NiMnGa single crystals," *Appl. Phys. Lett.* **83**, p. 3966, 2003.